48th AIAA Aerospace Sciences Meeting Including the New Horizons Forum and Aerospace Exposition
4 - 7 January 2010, Orlando, Florida
AIAA 2010-1216

Photogrammetric Measurement of Recession Rates of Low Temperature Ablators in Supersonic Flow

David W. Callaway*, Mark F. Reeder† and Robert B. Greendyke‡
Air Force Institute of Technology, Wright-Patterson AFB, OH 45433-7765

Ryan Gosse§
Air Force Research Laboratory, Wright-Patterson AFB, OH 45433

Ablative heat shields have been used to protect hypersonic vehicles during atmospheric reentry during the Apollo missions and could be used for future flight vehicles as well. Advances in computational models enable a large variety of vehicle shapes to be considered. However, it is exceptionally difficult to perform reliable tests at conditions which are representative of flight to validate the models. Historically, tests have been conducted on substitute materials at low temperatures to validate models, but even these tests can pose significant challenges. For example, most previous studies rely on model shape measured before and after tests or have relied on Schlieren photography for measuring changes in model profile only. Only recently has photogrammetry been used to quantify shape change in three dimensions for the ablative models. In our study, the AFIT Mach 3 pressure-vacuum wind tunnel was used in combination with models consisting of dry ice to collect ablation data for models of different shapes at stagnation pressures ranging from approximately 0.4 atm to 3 atm and stagnation temperatures equivalent to room temperature. High speed Schlieren photography was used for visualization, and the three dimensional shape change was quantified with sub-millimeter accuracy using laser dot photogrammetry. Results for one shape are compared to those computed using a computational model, which employs a finite-volume approach to solving the (3-D) Navier-Stokes equations, with the gas assumed to be at equilibrium, while employing an implicit solver accounting for the material response. Increased stagnation pressure led to larger material loss in the stagnation region of the model, as expected.

I. Introduction

WITH the resurgence of interest in hypersonic flight vehicles, research into the behavior of ablative heat shields has likewise increased. Since the 1970's, heat shield research in the US Air Force and NASA has been primarily focused on the development of reusable technologies such as the tiles on shuttle. Now, NASA has revisited the capsule-like design in its latest Aries vehicle and elected to return to an ablating heat shield instead of a fully reusable one. In a similar vein, the Air Force is investigating ablative heat shield material for hypersonic lifting bodies.

In 2004, a RAND Corporation survey of hypersonic wind tunnels found eleven national and three private tunnels capable of speeds above Mach 5 with test cross-sections of a foot or greater. This does not include commercially owned tunnels like those found at Lockheed and Boeing as those are not typically available for general research purposes. The study also determined that there were eighteen hypersonic tunnels available for research outside of the United States. To further limit the available facilities, each are aimed at a specific style of testing. For instance, the Langley tunnels are typically considered ideal for preliminary design where as the AEDC tunnels are generally used for production testing.[1]

*Graduate Student, Major, USAF, Air Force Institute of Technology, Dept. of Aeronautics and Astronautics, AIAA Member
†Associate Professor, Air Force Institute of Technology, Dept. of Aeronautics and Astronautics, AIAA Associate Fellow
‡Associate Professor, Air Force Institute of Technology, Dept. of Aeronautics and Astronautics, AIAA Associate Fellow
§Research Engineer, AFRL/RBAC, 2210 8th St B146 R225, Wright Patterson AFB, OH 45433, AIAA Member

The majority of work on ablative heat shields was performed in the 1960's and 70's during the heyday of the manned space program. The conditions under which heat shields operate are very difficult to produce and maintain in a test environment. To produce the high speed and high enthalpy conditions, an arc-jet set up is often used. An arc-jet uses an electric arc to heat the test medium as it is expanded in a converging-diverging nozzle to high supersonic speeds. These setups typically provide a few seconds to a few minutes of test conditions. [2]

These limitations are not new, and from the beginning of ablation heat shield research, efforts were made to find more economical means of testing ablation. As early as the 1950s, fundamental research into ablation was conducted using materials which undergo ablation at much lower temperatures and pressures than actual ablative materials. [3] Several efforts, of varying degrees of success, were made using dry-ice, water ice, and wax with the stagnation temperatures typical of that for a cold flow wind tunnel. [4], [5], [6], [7], [8], [9]

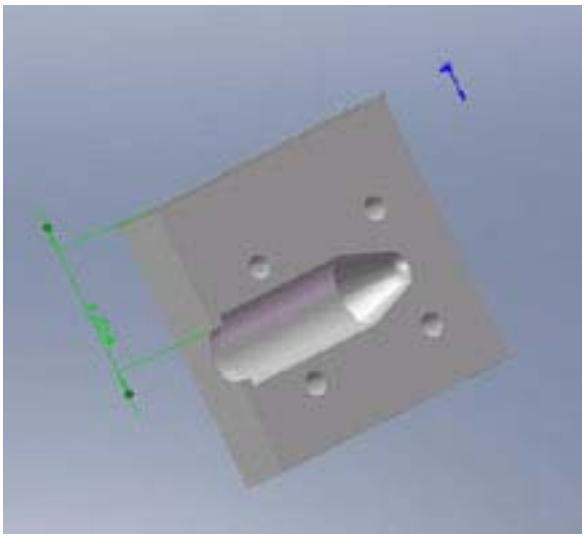

Figure 1: Solidworks image of spherically blunted cone mold

Many of these experiments were conducted by performing a wind tunnel test with measurements acquired before and after a test run. This approach provides the means to measure three-dimensional effects but prevents data from being accumulated during the experiments. Therefore, it can be difficult to determine whether tunnel startup and shutdown influence the measured recession rate. Schlieren visualization or film photography was also sometimes used to document the profile ablation during the run, but was of course limited to measurements of profiles as opposed to collecting three-dimensional effects.

With a reestablished interest in expendable ablative heat shields, coupled with many significant advances in measurement technology, improvements in these successes have prompted a renewed interest in ablation experiments. Schairer and Heineck demonstrated that three dimensional ablation rate measurements could be attained in an arcjet environment using Photogrammetric Recession Measurement (PRM), which they describe as a combination of particle image velocimetry and photogrammetry. They used two synchronized cameras to collect images of the test article at 15 Hz and performed cross-correlations to track the position of features on the test articles. One of their findings was that test articles with significant contrast in the surface texture provided the best results. [10]

Figure 2: Rapid prototype production of spherically blunted cone mold.

It was thought that a modified form of the technique used by Schrairer and Heineck might be applied to a low temperature ablation environment. To this end, work was performed at the Air Force Institute of Technology using the AFIT high speed wind tunnel facility to measure ablation rates on three-dimensional surfaces using dry-ice exposed to a Mach 3 free stream. The focus of the experiment is to support the development of a technique to model high temperature/high speed effects in flight by providing data which would serve as a benchmark for computational models.

II. Model Fabrication

The method used in this research forms the model directly from liquid CO2 in a mold of the prescribed shape. The description of the process by Kohlman and Richardson (1969) was investigated as a basis for this technique. In this method, liquid CO_2 is taken from high pressure to room pressure quickly. This rapid loss in pressure causes some of the CO_2 to flash freeze into dry-ice while the rest converts to gas. In a commercial process, this would be followed by compression. In the set up used for this experiment, the compression is supplied by the tank providing the liquid CO_2.

First, a Solidworks® model of the desired shape was produced as seen in Figure 1, followed by the production of a rapid prototype model as seen in Figure 2. The mold is made of rapid prototyping resin material. The material proved robust, handling liquid CO2 temperatures and pressures up to 300 psig. The molds were made as transparent as possible to aid in observation during model fabrication.

A feed pipe made of steel tubing with a 0.25inch outer diameter and an inner diameter of 0.12inch was used to bring in the liquid CO2 and double as the sting support in the wind tunnel. The outer surface of the pipe was threaded to allow for attachment hardware and an insulator material.

Liquid CO_2 is brought in through the pipe from a large tank called a Dewar and captured in the mold by the metallic filter. These metallic filters are produced by Mott Corporation out of 316L stainless steel. They can be machined, cut and are hydrophobic, so the liquid CO_2 is trapped but the filter allows out gassing. The filters come in a variety of porosities from 0.1 to 100 microns. Model fabrication started with the 100 micron filter, which was too porous to trap particulate dry-ice and produced slush. The 60 micron filter produced only slightly better results. The 40 micron filter produced models that looked complete, but when compared to the 20 micron filter models, it appeared less dense. Models with a 10 micron filter commonly had voids in the dry-ice which were believed to be caused by trapped gasses. So for the research presented here a 20 micron filter was determined to be the most effective for model production.

This method of producing a mold directly from liquid CO_2 provides the capability to run many tests on shapes that are extremely similar if not exact copies, increasing the data sets available for comparison. And by producing models in the wind tunnel, the time between tests is minimized. Obviously with dry ice, it is desired to keep the time between model production and tunnel operation to a minimum to reduce sublimation before testing. With this set up, testing as often as five times an hour was not uncommon and was limited primarily by the time needed for the

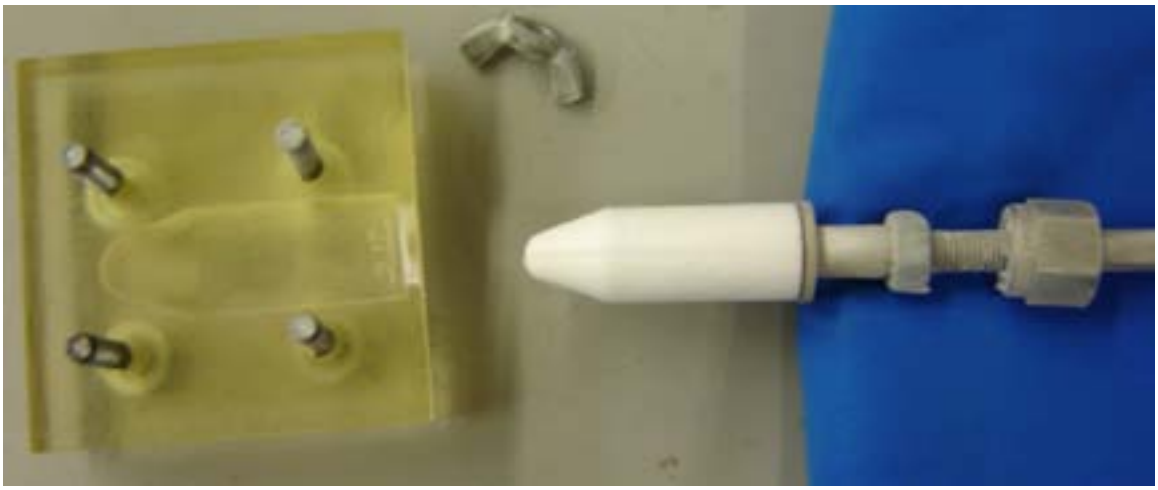

Figure 3: Dry-ice model after removal from mold during density measurements

vacuum pumps to evacuate the downstream tank. However, a separate issue arises when models are made rapidly as the CO_2 Dewar can lose overpressure if the liquid is siphoned out too rapidly. This will cause the liquid in the tank to flash freeze into dry-ice in the same process used to form the models. If the tank freezes, it takes days to thaw completely. Also, it was found for the molds used in these experiments that pressures less than 290 psi in the tank often led to large voids in the formed model, rendering the model unusable for ablation measurements.

Figure 3 shows a dry-ice model fresh out of the mold. This image shows the surface of a model well and the orientation on the sting used in the experiments. This particular image is from the density measurement and is taken outside of the wind tunnel. For the wind tunnel tests, the models were built in-situ. A length of pipe was curved and brought through the tunnel floor and provide both the liquid CO_2 and the sting. In Figure 4 a mold in the wind tunnel provides an example of the set up with insulator, filter, spacer, and nut. The insulator is positioned between the dry-ice model and the steel tube in order to minimize heat transfer from the tube to the model. The filter also has small fins to provide stability to the model.

It is clear from Figure 3 that the dry ice models do not exhibit significant surface texture. Therefore, rather than using the natural features of the model to determine recession, laser dot projection photogrammetry was applied. A variation of this technique is described in reference [11].

The most productive technique found for model fabrication was as follows. The valve to the liquid CO_2 on the Dewar would be turned on half a turn or until the pressure relief valve began blowing off. Once liquid was flowing, which was visible as a large cloud of condensation coming from the mold or relief valve, the valve was opened one more full turn. The translucent mold material offered an advantage in that the liquid could be seen solidifying, and with some practice of the procedure it was often possible to tell when the model had fully solidified. The model was observed for fullness, and the pressure gauge was monitored for back pressure build up. Once either of these two outcomes were observed, the valve was closed and the mold disconnected. The mold was then opened and the model inspected for surface defects. If no defects were observed, the tunnel walls were replaced and the wind tunnel was operated. The time between when the models were inspected and when the tunnel was operated was typically about 30 seconds. This short time was necessary due to the rather high sublimation rate of dry ice at room temperature and pressure.

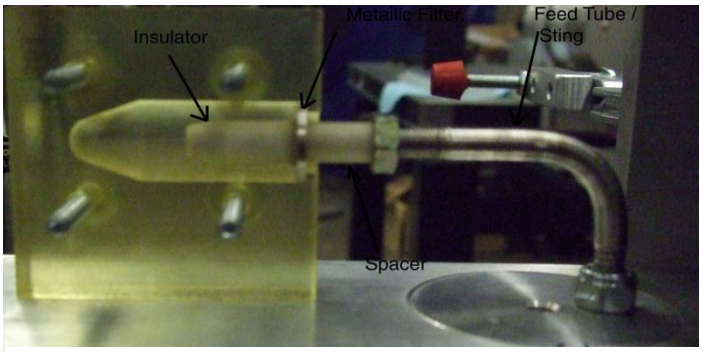

Figure 4: Mold in wind tunnel

Once the technique was mastered, density measurements were made outside of the wind tunnel and are provided in Table 1. To generate the density measurements, the volume of the mold was first determined using distilled water. Measurements were taken, and the volume was found to be 6.11 cm^3. Dry-ice models were then formed and their mass measured to find the mass of the dry-ice.

Eight visibly flawless models were used to determine the mass of the models with a 20 micron filter, which was used for all of the results presented in this paper. For comparison, the average of samples formed using a larger (40 micron) filter is given to demonstrate that, as anticipate, the filter choice can influence the density of the dry ice. It should be noted that commercial grade dry-ice is approximately 1.5 g/cm^3, so the formed dry ice used in our experiments is about 30% less dense than most commercially available blocks.

	Average (g/cm^3)	Range (g/cm^3)
Density (20 Micron)	1.0051	0.9761-1.042
Density (40 Micron)	0.9395	0.9122-0.9581

Table 1: Dry-ice densities

III. Experimental Equipment and Test Procedures

The wind-tunnel used for this experiment, part of the AFIT blow-down facility, has been in use since the mid to late 1990's. The test section is 6.4 x 6.4 cm (2.5 in x 2.5 in). There are currently two convergent-divergent nozzles capable of producing nominally Mach 1.8 and Mach 3 conditions in the test section. For the purposes of this research, only the Mach 3 nozzle was used, and it typically led to a measured free stream Mach number of 2.94.

Pressure transducers are used to record the mean stagnation chamber pressure as well as the mean free stream pressure in the test section. Figure 5 shows the tunnel with the three cameras used for photogrammetry set up in order to capture a small angle of attack run. In practice, Mach 2.94 flow can be produced for approximately 20 to 30 seconds. [12]

Test conditions for the research presented here were Mach 2.94 with a stagnation temperature of 290K, and a static temperature of 107K. A significant advantage of the system is that the wind tunnel can be operated with stagnation tank pressures ranging from 10 to 50 psia, and thus can change the dynamic pressure and Reynolds numbers of the flow.

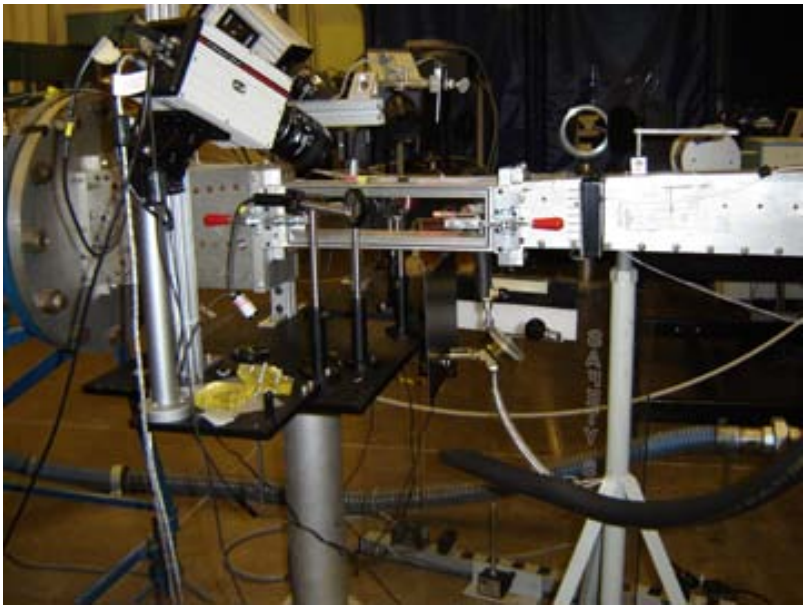

Figure 5: AFIT blow down facility with cameras set up for 0 angle of attack experiments

Three MotionPro X-series high speed cameras with Nikkor 60mm f/2.8D lenses were used for model imaging. The X-series are designed for use in industrial and research applications that involve motion evaluation. The cameras are synchronized and connected to a computer via a USB 2.0 digital interface and are capable of 5000 frames per second at full resolution (1024 pixels by 1024 pixels). [13] For the data presented here, the images were recorded at 1000 frames per second with an 885 microsecond exposure.

In order to collect meaning data, at least two cameras must contain any given feature. The three cameras were generally positioned to yield data for the upper half of the model, including the stagnation region at the upstream portion of the model. The Motion Studio software suite is used to control the cameras as well as record and manipulate images.

In addition to the photogrammetry, Schlieren images were taken with a Photron Fastcam at 1000 Hz. These images were primarily used to determine when the tunnel had reached steady flow conditions, which was found to be between half a second and one second after the high pressure system was released. They also provided useful immediate qualitative feedback on the recession of the test articles. Comparison of Schlieren images can be seen in Figure 6 and Figure 7 presented for two different shapes at three different stagnation pressures at four instants in time (presented in one-second intervals).

Figure 6 is a set of images taken of a spherically blunted cone, spaced out at one second intervals vertically. The horizontal columns represent the same shape at three different stagnation pressures, as annotated in the chart. The lowest stagnation pressure is 6.1 psia, the middle at 23.0 psia, and the highest stagnation pressure at 45.7 psia. A primary interest here is to visibly show that higher pressures ablate at higher rates, and is evident obviously in these images. It should be pointed out that the nose of the high pressure images is intact, but some interaction of the shock waves is causing a bright spot to develop. Starting just after the last time step shown here, a forward cavity appears to develop, though it is somewhat exaggerated due to optical aberration.

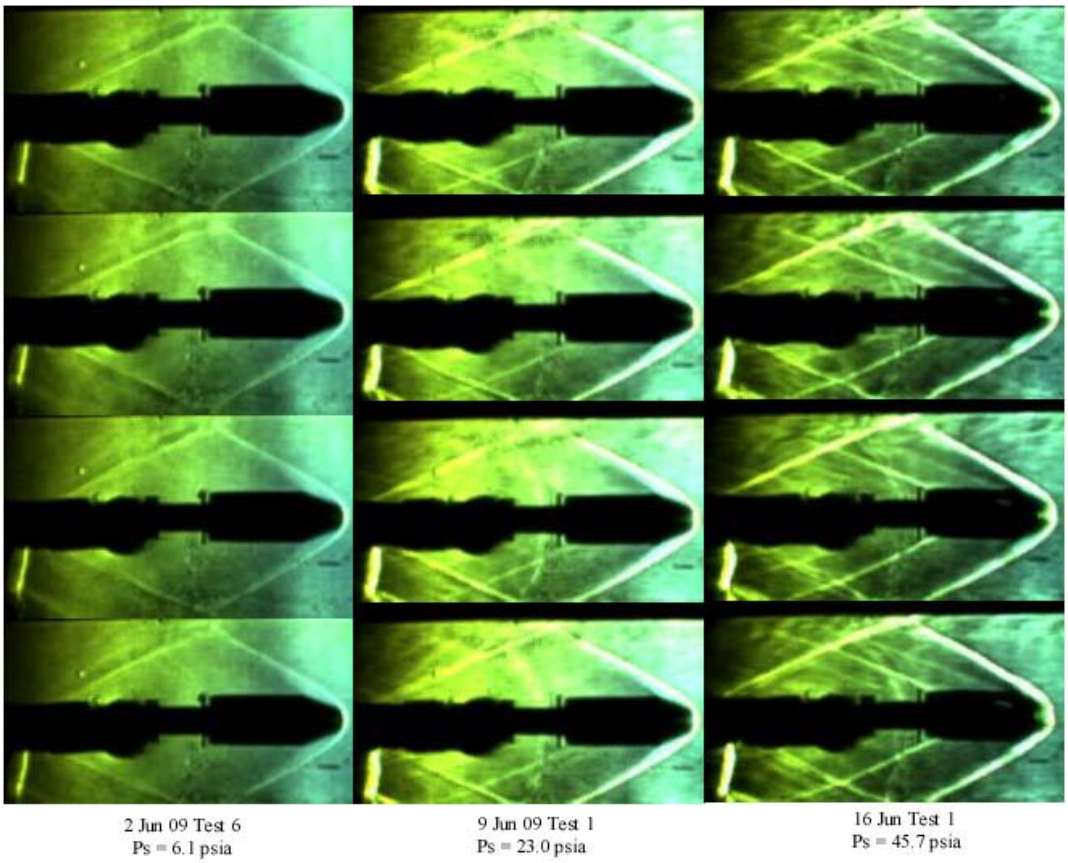

Figure 6: Spherically blunted cone at three different pressures and one-second time intervals

Figure 7 has the same format as Figure 6, but in this figure the shape tested is a spherically blunted cylinder. The differences in the shock waves are obvious from the much blunter body, and again, the higher pressures visibly show higher ablation rates. The high pressure run, at 46.9 psia stagnation pressure, shows the beginning of deformations in the nose area in the last image of the sequence. This is due to a large shape change in the nose area most likely due to a defect in the ice. In these cases, the three-dimensional data would stop on the last frame prior to a defect emerging. Most of the three dimensional data presented in this paper is based on the spherically blunted cone design, but this image is provided to show comparisons of test runs.

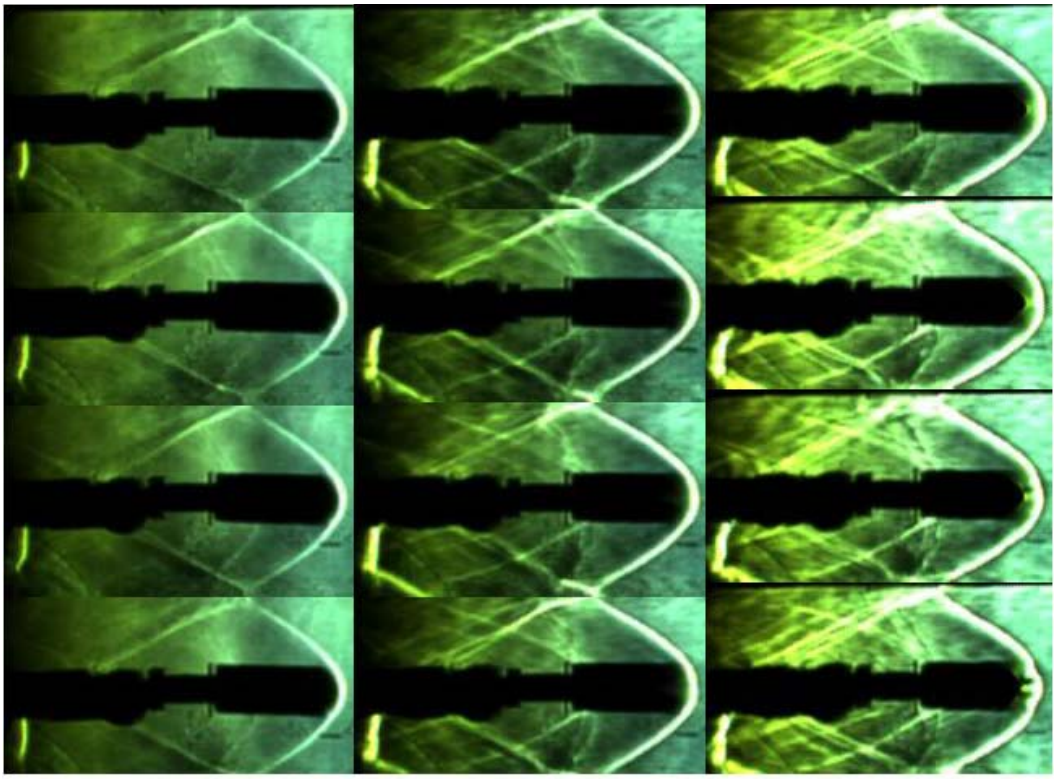

Figure 7: Spherically blunted cylinder at three different pressures and one second intervals

The Schlieren visualization proved to be an extremely valuable tool in guiding the research. For example, early in the research program, images from tests showed that some models were too large for the tunnel for the tunnel to start. Likewise, in tests acquired with model at an angle of attack, the Schlieren visualization indicated the location of shock wave interaction with the model and wall reflections.

After the cameras were set up, the laser grids were set up to project onto the surface of the model. Three lasers were used for the majority of this research. The lasers were fitted with grid filters that produced a grid of 7x7 individual points. Two laser grids were projected at an angle onto the front of the model from either side of the wind tunnel. Convex optics with a focal length of 120 mm were used to produce smaller grids and therefore finer grids on the model surface. A third laser was pointed perpendicular from above onto both the model and the wind tunnel floor. The grid points on the floor were used as anchor points from image to image and provided the scale of the wind tunnel. This grid was checked daily and after any adjustments to maintain a 6 mm grid on the floor of the tunnel. A fourth laser was added in the higher angle of attack test runs to produce a finer grid on the model.

To visualize the model in the wind tunnel, refer to Figure 8. The top left image in is an image of a dry-ice model in the wind tunnel without the lasers on. The center left image provides a view of the model with the laser grids projected onto it. The grid projected from above also projects onto the floor of the tunnel. Care was taken to collect these points on the floor of the tunnel with all three cameras in order to provide stationary reference points necessary for data processing. The remaining images in Figure 8 are raw images taken with the MotionPro X-series cameras during a wind tunnel run.

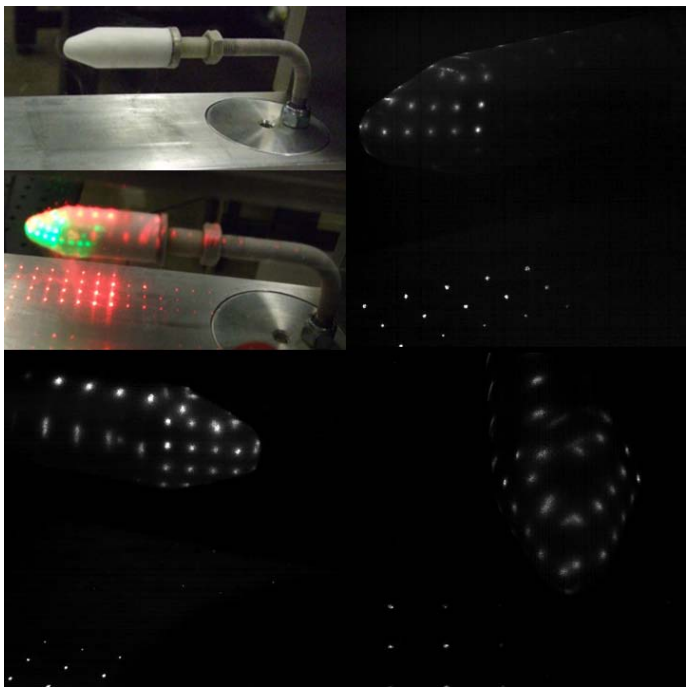

Figure 8: Raw images of dry-ice model in wind tunnel. Counter clockwise from top: image of model in tunnel, image with lasers on, starboard side of model, top of model, port side of model

After the run, the images were imported into PhotoModeler in order to extract measurements and produce three-dimensional computer models from photographs. The software is robust, and can be used with images from unknown sources, known camera specifications, or cameras that are calibrated by PhotoModeler during imaging. For curved surfaces, three camera angles are preferred from as near to a 90^{o} offset as possible, which includes vertical and horizontal planes. The program is designed for use in such areas as accident reconstruction, architecture, preservation, archeology, forensics, film, games, animation production, and modeling for engineering, industrial and experimental applications.

For capturing shape change of an object, the PMV (PhotoModeler Video) module was utilized. This module also automatically tracks target points, for example laser grid points in this research, across the time frames for improved efficiency. [14] While the automation of the software is useful, each frame must be manually inspected by the user to insure accuracy in point tracking and locations.

Three-dimensional coordinates of the points were typically tracked using this approach over times which varied from as low as three seconds for high pressure experiments up to about 12 seconds for low pressure experiments. . The imported images can be seen in Figure 9 for an initial time and final time.

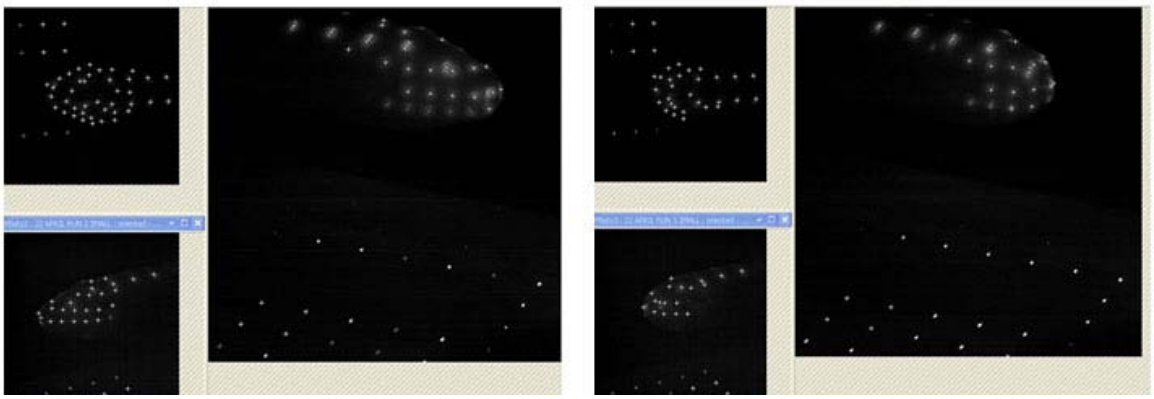

Figure 9: Image capture in Photomodeler. Initial time on the left and final time on the right.

Figure 10 shows a rendering of the three-dimensional points resulting from processing via PhotoModeler with a three dimensional representation of the grid points. These images can be rotated and viewed in all time epochs processed. The coordinates and residuals of the point cloud can be exported in a text file of three dimensional data points along with the residuals of each point. The residual is the disagreement between the cameras that can detect the point and provides a measurement of the accuracy of the approach.

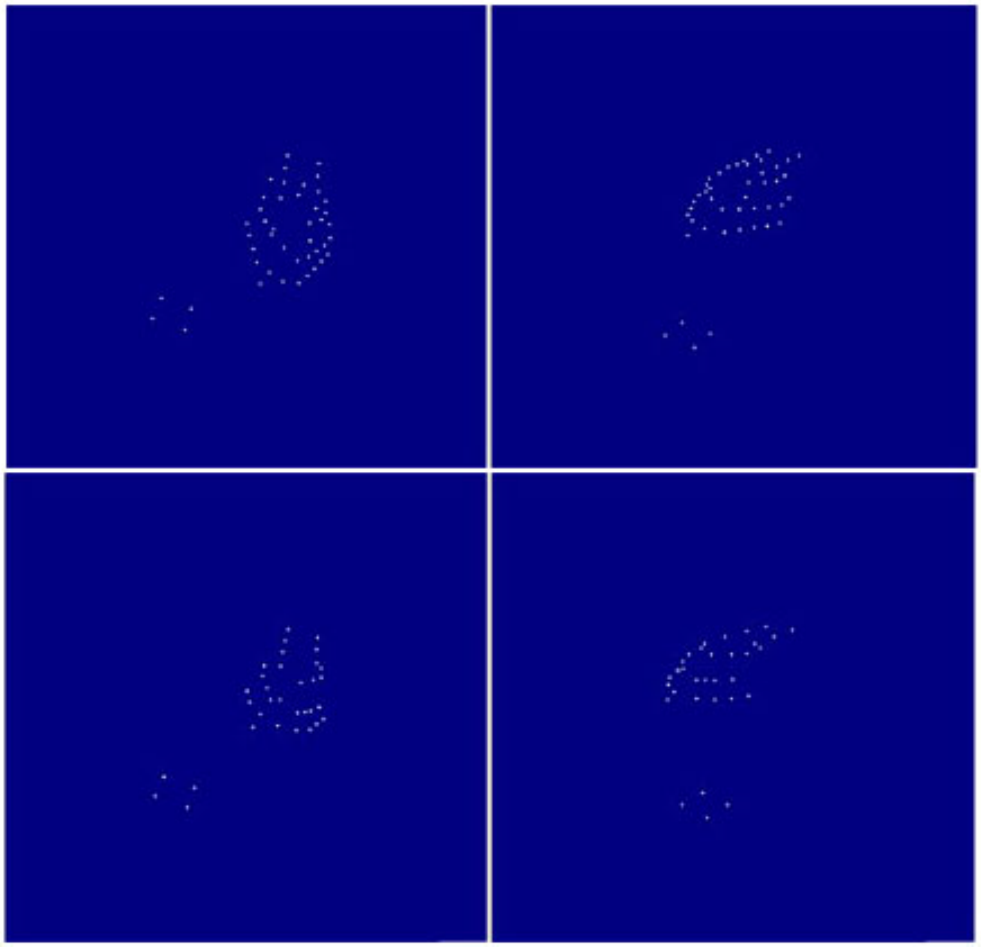

Figure 10: PhotoModeler image of initial 3-D data (top) and final time position 3-D data (bottom)

IV. Experimental Results

The data gathered in the process described above is exported as a table of individual three dimensional points at each time step. These points are then imported into Matlab and plotted for visual comparisons. All data sets presented in this section are spaced out at 1 second intervals unless otherwise indicated.

Several experiments were conducted to determine tunnel noise, or the error one could expect from the tunnel's vibrations. For the experiment presented here, the closest wind tunnel test was at a stagnation pressure of 16 psia. The average movement of the test article can be found in Table 2.

Axis	Average change in mm	Standard Deviation
X	0.05589	0.02228689
Y	0.03543	0.02074373
Z	0.0811	0.025915847

Table 2: Wind tunnel noise experiment at stagnation pressure of 16 psia

The following images (Figure 11 - Figure 13) represent a single test of a spherically blunted cone. This is the same test shown as the low pressure run in Figure 6. The conditions of this test are given in Table 3.

Mach	2.94
Stagnation Pressure (psia)	6.15
Stagnation Temperature (K)	291.4
Average Residual (mm)	0.027
Minimum Residual (mm)	0.0002
Maximum Residual (mm)	0.1061

Table 3: Test conditions for a spherically blunted cone model

The first image (Figure 11) shows a top down surface map of the model at one second intervals. In this figure, the original position is black and the position at the time step is shown in red. In Figure 12, the results are presented from the top view, which shows where point lie on the x-y plane. The original position point represented as circles and the current time position with an "x."In Figure 13, the same results are from a side view of the x-z plane (left) and from a frontal view of the y-z plane. Using the pointwise representation, it is somewhat easier to see the change in shape over time looking at the three views.

In Table 4, the changes in position of this test are given for comparison. The fact that the lasers are at an angle to the model is apparent in the movements of y and z, and should be taken into account. For this reason, treating the data as a surface can be beneficial. However, by observing the data points, one can glean the change in one direction of the model. In this instance, the change in the x-direction of the nose can be calculated directly from the point represented on the nose.

:

X (mm)	Y (mm)	Z (mm)
0	0	0
-0.0484	-0.0604	-0.0107
-0.0572	-0.126	-0.0204
-0.0756	-0.0583	0.0444
-0.1151	-0.1249	-0.0733
-0.2128	-0.2665	-0.0794
-0.1959	-0.2553	0.0192
-0.2269	-0.3276	0.0065
-0.2716	-0.3864	-0.0555
-0.3825	-0.4338	-0.0812
-0.3325	-0.5485	0.0262
-0.3728	-0.3756	-0.0701
-0.4245	-0.5662	-0.0077
-0.4811	-0.6358	0.0205
-0.5718	-0.6838	0.0254
-0.681	-0.6494	0.0652

Table 4: Change in position of a point on the nose of spherically blunted cone at stagnation pressure 6.1 psia.

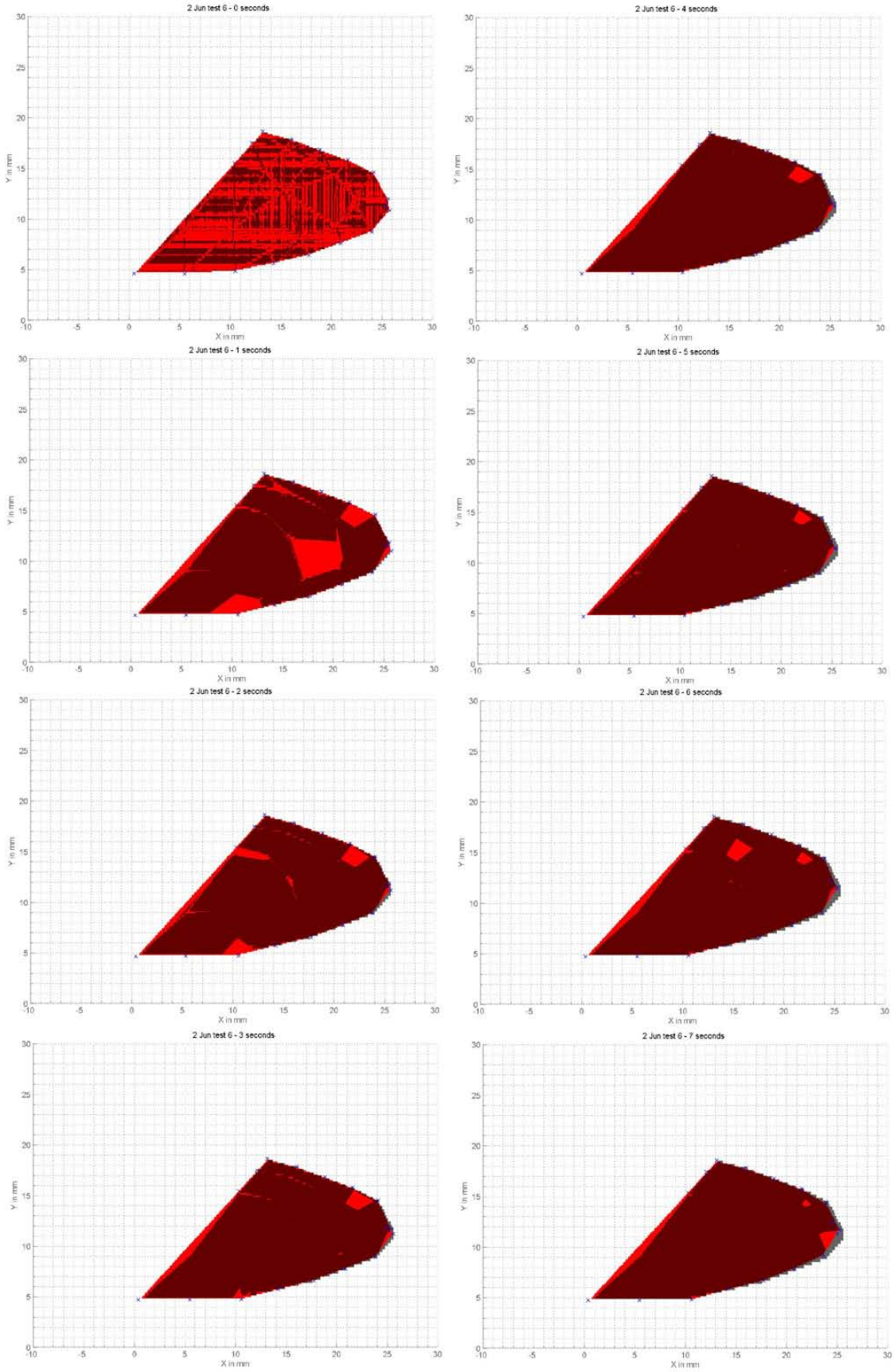

Figure 11: Spherical Cone Model with a stagnation pressure of ~6.9 psia surface plots

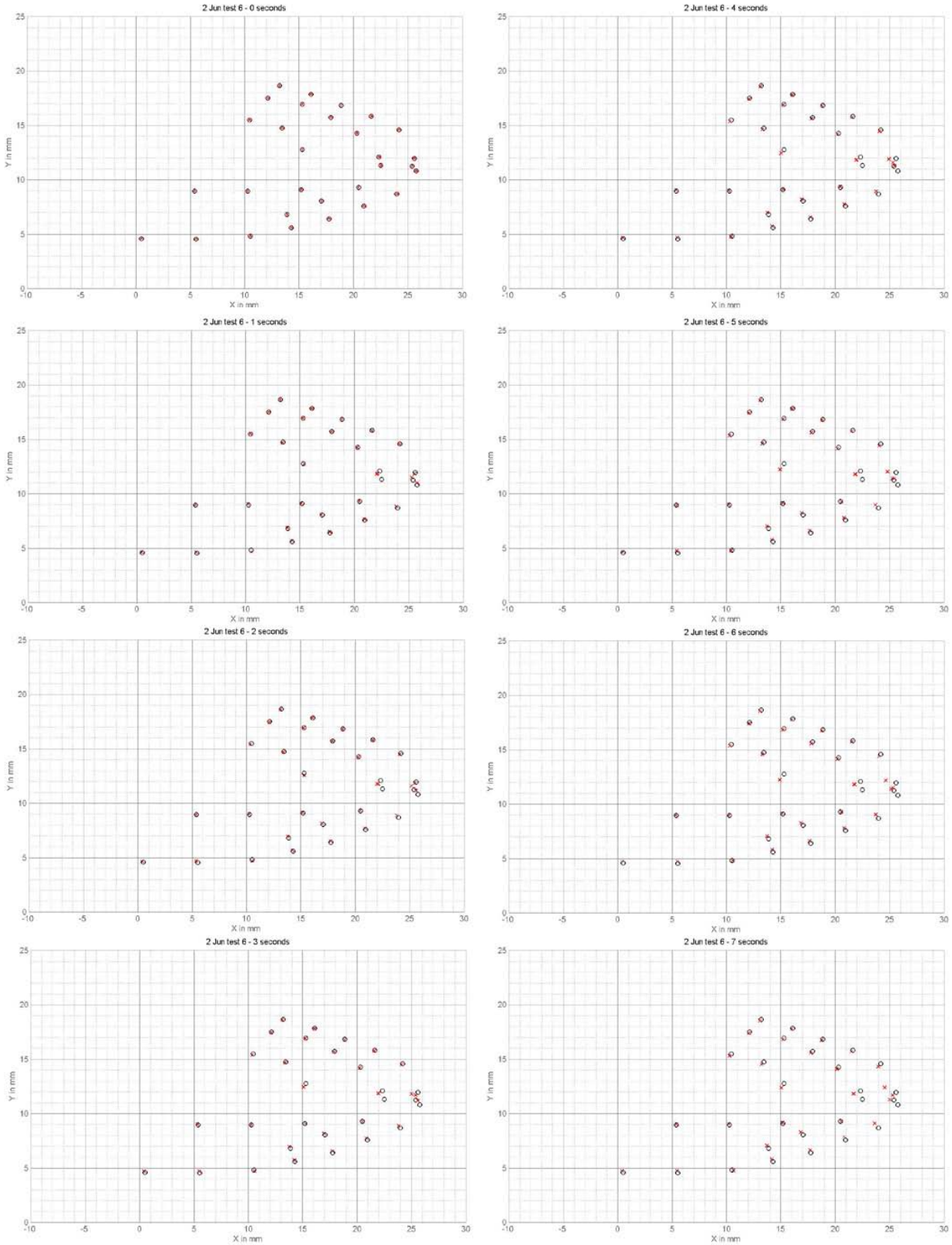

Figure 12: Spherical Cone Model with a stagnation pressure of ~6.9 psia 3d point plots top view

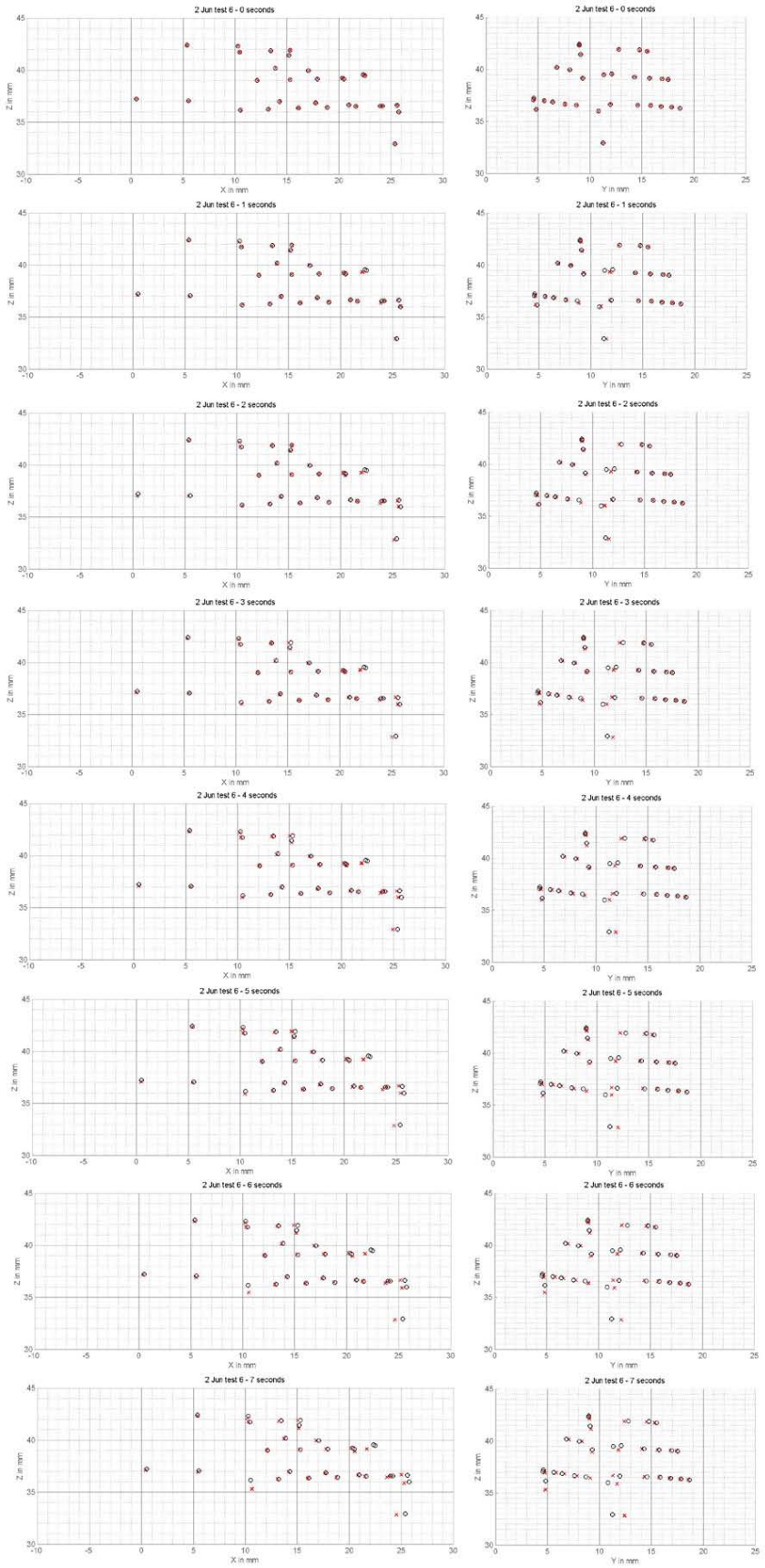

Figure 13: Spherical Cone Model with a stagnation pressure of ~6.9 psia 3d points side and front views

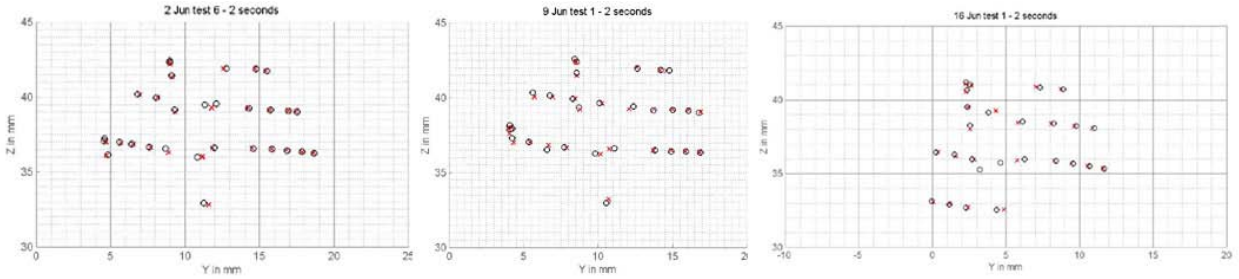

Figure 14: Comparison of low, medium, and high stagnation pressures: front view

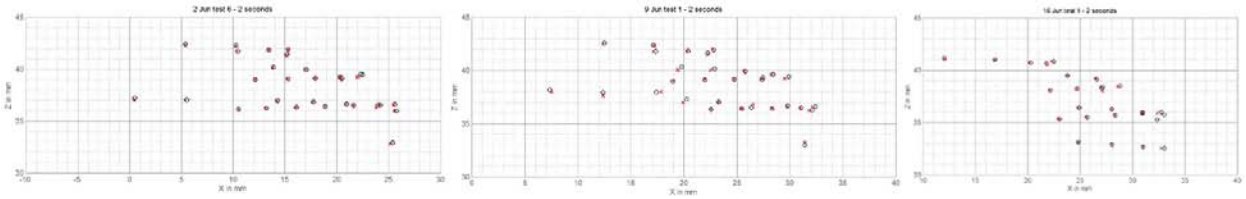

Figure 15: Comparison of low, medium, and high stagnation pressures: side view

Figure 14 through Figure 17 present comparisons of the same spherically blunted cone shape at three different stagnation pressures: 6.1 psia, 23.0 psia, and 45.7 psia with only the starting point (t = 0 seconds) and ending point (t = 2 seconds) of the experiments shown. Figure 14 is a comparison of a view from the front, Figure 15 is a view from the side; and Figure 16 is a view from above. Figure 17 represents the surface rendering.

Stagnation Pressures (psia)	6.1	23.0	45.7
$\Delta x/\Delta t$ (mm/s)	-0.091	-0.157	-0.192
$\Delta y/\Delta t$ (mm/s)	-0.087	0.0343	-0.250
$\Delta z/\Delta t$ (mm/s)	0.0087	-0.0536	-0.0364
Average Residual of point (mm)	0.040	0.0198	0.0187

Table 5: Comparisons of nose tip recession rates of spherically blunted cones with stagnation pressures of 6.1, 23.0, and 45.7 psia

In Table 5, comparisons of nose tip recession rates are shown between the different pressures along with the camera residuals of the points. It should be emphasized that the most valuable rate is given by the first row ($\Delta x/\Delta t$). The remaining two rows may show the influence of the direction of the laser beams entering the test section. The data confirms the anticipated result of higher stagnation pressure leading to higher recession rates.

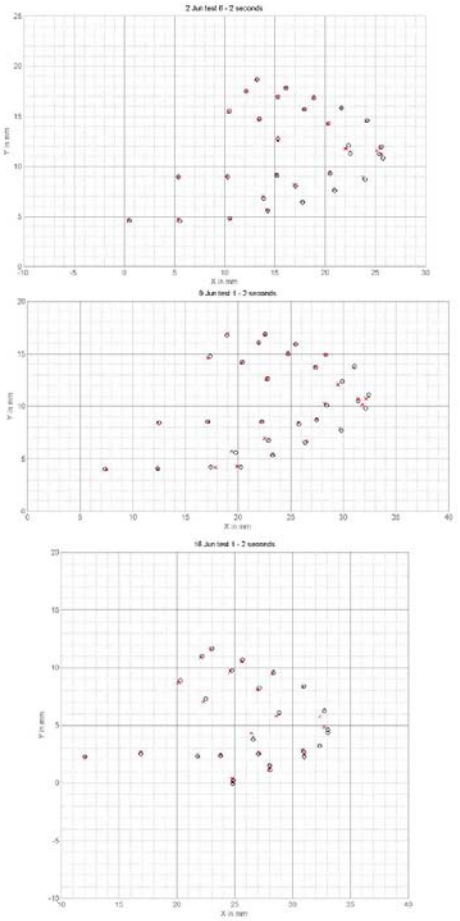

Figure 16: Comparison of low, medium, and high stagnation pressures: top view

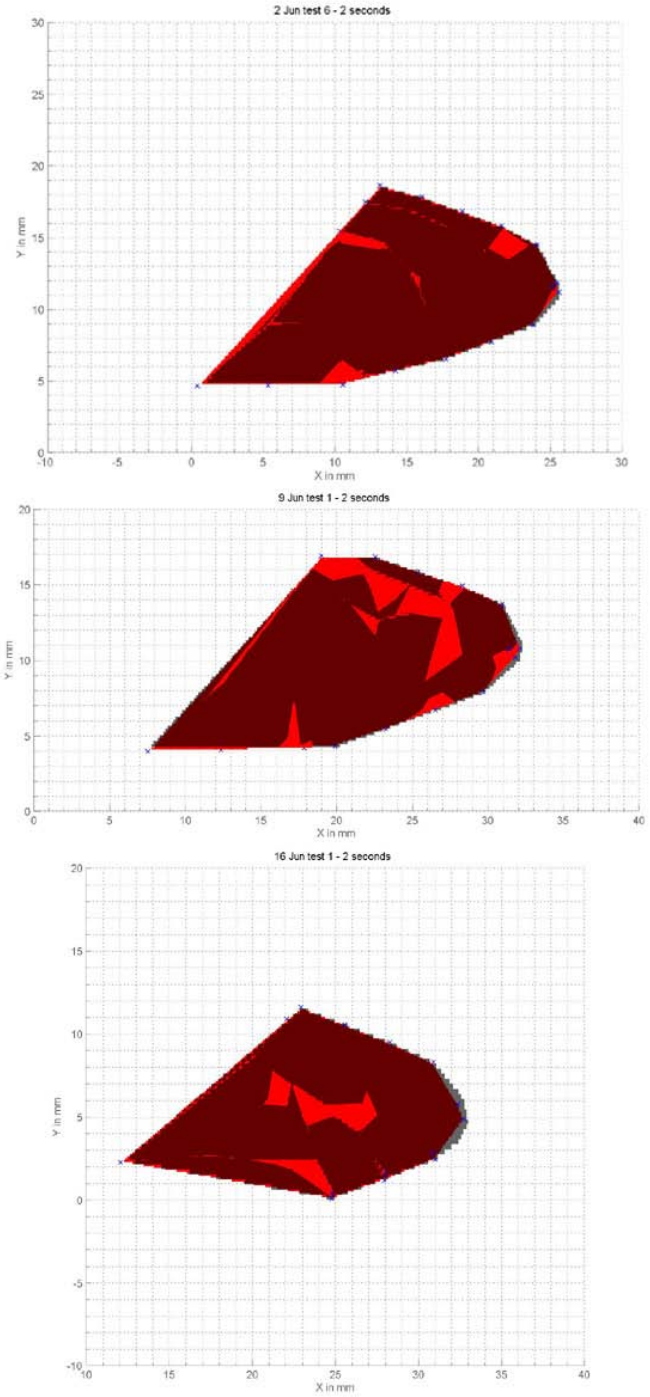

Figure 17: Comparison of low, medium, and high stagnation pressures: surface top view

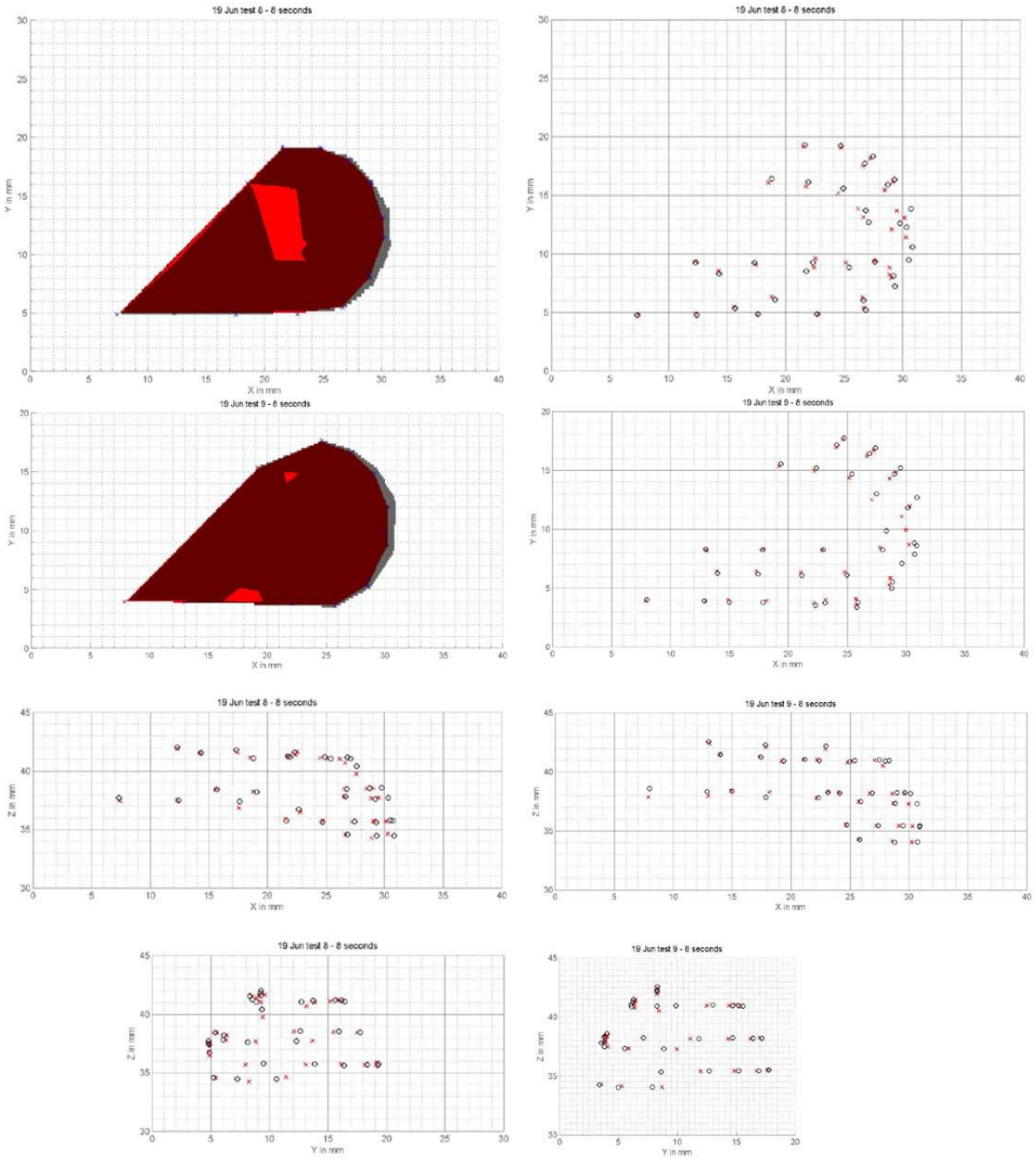

Figure 18: Comparison of two low pressure runs for similarity

Repeatability is a addressed by comparing two runs for the sphere-cylinder conducted at the same stagnation pressure in Figure 18. While there are some differences in the shape of the model, the nose tip recession rate is within 10% and less than the residual errors from the cameras. This data is presented below in Table 6.

Test:	9 Jun test 8	9 Jun test 9	Difference
dx/dt (mm/s)	-0.0691625	-0.0609875	-0.008175
dy/dt (mm/s)	0.1048875	0.10145	0.0034375
dz/dt (mm/s)	0.017475	-0.0031625	0.0206375
Average Residual of point (mm)	0.014588235	0.022164706	-0.007576471

Table 6: Comparison of similar tests on spherically blunted cylinder

V. Computational Modeling

The equilibrium ablation CFD solver was developed by the University of Minnesota. It is an evolution of an unstructured extension of NASA's data-parallel line relaxation method (DPLR) implemented in a multi-block structured grid. [15]

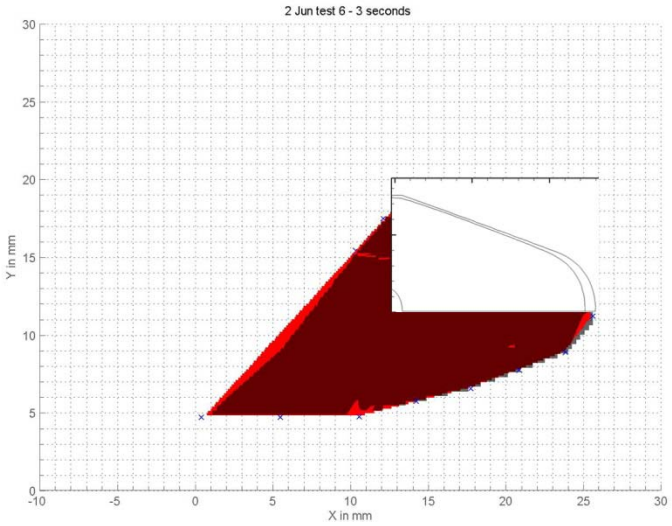

Figure 19: Comparison of CFD to experimental results at time elapsed 3 seconds

The details of the solver were presented by Nompelis, Candler, and Conti. [16] In this paper, only a brief outline of the solver will be presented. To model the ablation process, the CFD solver consists of four separate methods. The fluid domain is modeled by two methods. The gas phase elements are modeled using the Navier-Stokes equations with a thermodynamic equilibrium formulation (instead of a state equation for pressure). The equations consist of multiple continuity equations, momentum conservation in three dimensions, and the total energy equation. A surface boundary condition is required between the fluid and solid domain to account for the process of ablation and heat transfer at the surface. The condition is satisfied by mass and energy balance equations.

There is one missing condition to determine the gas chemical state on the surface. This is usually obtained with a "B-prime curve" that plots the ratio of ablation product element gas to air gas (two elements) for an equilibrium mixture as a function of pressure and temperature. In the case of sublimation of CO2, the B-prime value can be found knowing the equilibrium vapor pressure. For a given state of the gas at the surface, the partial pressure of the CO2 will match that of the equilibrium vapor pressure. If the partial pressure of CO2 is higher, then the CO2 will condense into a solid. If the partial pressure is lower, the solid CO2 will sublime from the surface to reach an equilibrium state. For general ablation problems where the ablation process is dominated by oxidation or another limiting process, B-prime tables are used to set the rate of ablation. The details underlying this approach is based on a long line of evolution through implicit CFD solvers developed by MacCormack [17], Conti and MacCormack [18], Candler and MacCormack [19], Wright et al [20], and Nompelis et al [21]. Gas composition and associated thermodynamic variables are solved using a specialized equilibrium gas solver based on the approach of the NASA CEA (chemical equilibrium analysis) code. NASA's CEA code calculates equilibrium product concentrations from a set or reactants and determines thermodynamic and transport properties using a minimization-of-free-energy approach. It was designed to apply to a wide range of problems, such as the design and analysis of compressors, turbines, nozzles, engines, shock tubes, heat exchangers, and chemical processing equipment. [22] The CEA code is written in ANSI standard FORTRAN 77 and contains more than 2000 species in its thermodynamic database. [23]

The CFD solver was developed to model carbon ablation phenomena and required modifications to account for the CO_2 ablation process. As indicated above the B-prime curves were calculated using the thermodynamic properties of CO_2 dry-ice. The dry-ice typically experiences larger amounts of ablation than carbon materials. This caused some issues with the CFD solver. The implicit Jacobians at the surface are computed numerically and rely on a smooth function of the ablation rate over surface temperature and pressure. The larger blowing rate seems to cause an instability issue in the code which requires a small CFL value to be used. For the carbon ablation modeling CFL numbers over 1 million can be used. For the dry-ice case values close to 1 were required. This reduced the practical amount of time in which a computation can be conducted. Some preliminary results were given in reference [24].

VI. Comparison of Experiment and Computational Modeling

Limited comparisons are provided to demonstrate that the experimental and computational results correspond reasonably well. Results for the streamwise position of a point at or near the stagnation point of the sphere-cone model for three different stagnation pressures are given in Figure 20, Figure 21, and Figure 22. It should be emphasized that the experimental results for this single point do not strictly adhere to the center of the model. The correspondence of the CFD model to the experimental data is respectable, particularly for the two lower pressure cases. This data is somewhat preliminary, and more analysis is required to ascertain the level of correspondence for the three dimensional shape.

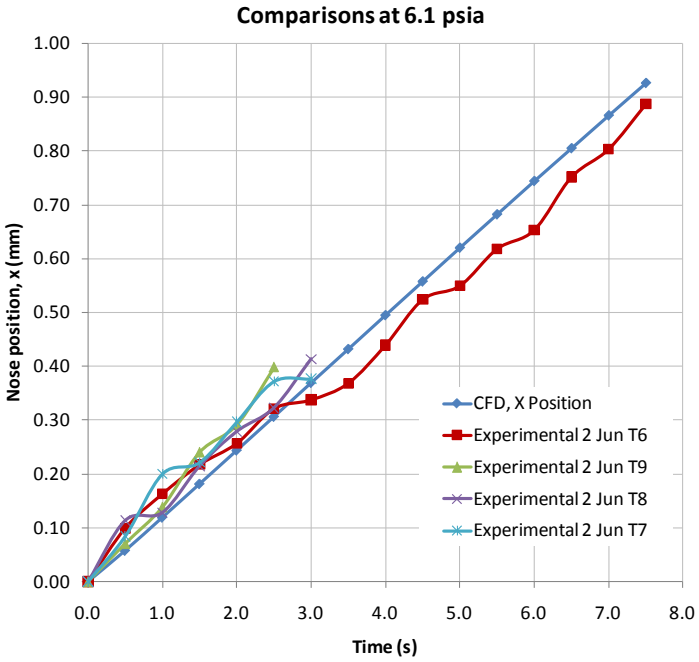

Figure 20: Comparison of experimental and computational ablation at 6.1 psia.

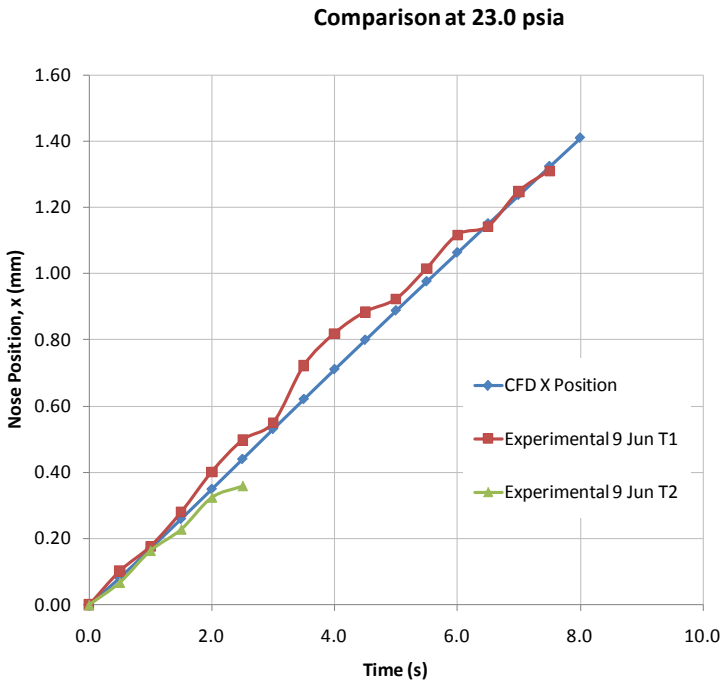

Figure 21: Comparison of experimental and computational ablation at 23 psia.

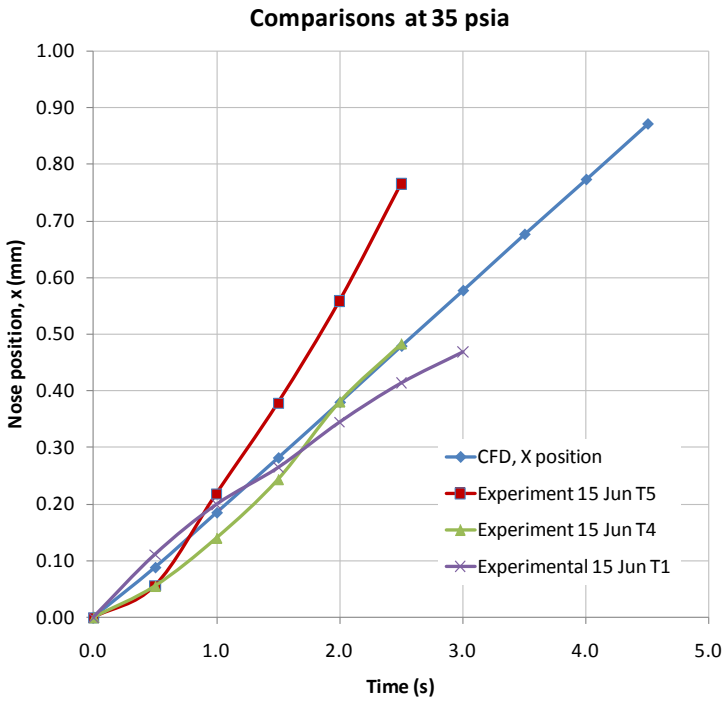

Figure 22: Comparison of experimental and computational ablation at 36 psia.

VII. Summary

An experimental program has been conducted at the Air Force Institute of Technology with the goal of quantifying ablation rates at low temperatures using appropriate ablative materials exposed to high speed flow conditions. The primary goal of the program is to develop a viable measurement technique of ablation rate which can be used to compare results to computational models.

The results are promising and the comparison to computational results is ongoing for a variety of different conditions and shapes. The AFIT Mach 3 pressure-vacuum wind tunnel was used in combination with models consisting of dry ice to collect ablation data for models of different shapes at stagnation pressures ranging from approximately 0.4 atm to 3 atm and stagnation temperatures equivalent to room temperature. High speed Schlieren photography was used for visualization, and the three dimensional shape change was quantified with sub-millimeter accuracy using laser dot photogrammetry. Results for one shape are compared to those computed using a computational model, which employs a finite-volume approach to solving the (3-D) Navier-Stokes equations, with the gas assumed to be at equilibrium, while employing an implicit solver accounting for the material response. Increased stagnation pressure led to larger material loss in the stagnation region of the model, as expected.

VIII. Acknowledgments

The authors would like to thank AFRL/RBAC for financial support of this project. We would also like to thank Jay Anderson, Chris Zickefoose, John Hixenbaugh and the rest of the lab support team for their invaluable guidance during wind tunnel set up and operations. This is AIAA paper 2010-1216.

The views expressed in this article are those of the author and do not reflect the official policy or position of the United States Air Force, Department of Defense, or the U.S. Government.

IX. Works Cited

[1] Philip S. Antón et al., "Wind Tunnel and Propulsion Test Facilities: Supporting Analyses to an Assessment of NASA's Capabilities to Serve National Needs," Santa Monica, CA, 2004.

[2] Peter Sherrouse, J. Sheeley, J. Mansfield, and D Rotach, "Design and Testing of a Zero-Focus Shadowgraph System for Ablation Measurement During Arc Jet Testing," in *36th AIAA Thermophsyics Conference, AIAA 2003-4046*, Orlando, 2003, p. 8.

[3] David E. Anderson, "Investigation of Ablation of Ice Bodies in Hypersonic Flows," California Institute of Technology, Pasadena, CA, Thesis 1960.

[4] David L. Kohlman and Richard W. Richardson, "Experiments on the Use of Dry Ice Ablating Wind-Tunnel Models," *Journal of Spacecraft and Rockets*, vol. 6, no. 9, Sept 1969.

[5] Fred Lipfert and John Genovese, "An Experimental Study of the Boundary Layers on Low-Temperature Subliming Ablators," *AIAA Journal*, pp. 1330-1337, 1971.

[6] Ching Jen Chen, "Low Temperature Simulation of Subliming Boundary-Layer FLow in Jupiter Atmosphere," *AIAA Journal*, pp. 259-267, 1978.

[7] Y. Ma, W.K. Van Moorhem, and R.W. Shorthill, "An Experimental Investigation of Velocity Coupling in Combustion Instability," in *28th Aerospace Sciences Meeting*, Reno, 1990.

[8] Sidra I. Silton and David B. Goldstein, "Ablation Onset in Unsteady Hypersonic Flow About Nose Tip with Cavity," *Journal of Thermophysics and Heat Transfer*, vol. 14, no. 3, pp. 421-434, 2000.

[9] Sidra I. Silton and David B. Goldstein, "Optimization of an Axial Nose-Tip Cavity for Delaying Ablation Onset in Hypersonic Flow," in *41st Aerospace Sciences Meeting and Exhibit, AIAA 2003-0152*, Reno, NV, 2003.

[10] Edward T. Schairer and James T. Heincek, "Photogrammetric Recession Measurements of Ablative Materials during Arcjet Testing," in *45th AIAA Aerospace Sciences Meeting and Exhibit, AIAA 2007-1158*, Reno, 2007.

[11] R.S. Pappa et al., "Dot-Projection Photogrammetry and Videogrammetry of Gossamer Space Structures," *Journal of Spacecraft and Rockets*, vol. 40, no. 6, pp. 858-867, 2003.

[12] S. Bjorge, M. Reeder, C. Subramanian, J. Crafton, and S. Fonov, "Flow Around an Object Projected from a

Cavity into a Supersonic Freestream," *AIAA Journal*, vol. 43, no. 7, pp. 1465-1475, 2005.

[13] Integrated Design Tools, Inc, Motion Studio Cross-Platform User Manual, June 2008.

[14] Eos Systems Inc., PhotoModeler 6 User Guide, Jan 2007.

[15] M. Barnhardt and G.V. Candler, "Deteached Eddy Simulation of the Reentry-F Flight Experiment," in *46th AIAA Aerospace Sciences Meeting and Exhibit, AIAA 2008-0625*, Reno, NV, 2008.

[16] I. Nompelis, G. Candler, and R. Conti, "A Parallel Implicit CFD Code for the Simulation of Ablating Re-Entry Vehicles," in *AIAA 2009-1562*, 2009.

[17] R.W. MacCormack, "Current Status of Numerical Solutions of the Navier-Stokes Equations," in *23rd Aerospace Sciences meeting, AIAA 1985-0032*, Reno, NV, 1985.

[18] R.J. Conti and R.W. MacCormack, "Inexpensive Navier-Stokes Computation of Hypersonic Flows," in *26th Thermophysics Conference, AIAA 1991-1391*, Honolulu, HI, 1991.

[19] G.V. Candler and R.W. MacCormack, "The Computation of Hypersonic Ionized Flows in Chemical and Thermal Nonequilibrium," *Journal of Thermophysics and Heat Transfer*, vol. 5, no. 3, pp. 266-273, July 1991.

[20] M.J. Wright, D. Bose, and G.V. Candler, "A Data-Parallel Line Relaxation Method for the Navier-Stokes Equations," *AIAA Journal*, vol. 36, no. 9, pp. 1603-1609, Sept 1998.

[21] I. Nompelis, T.W. Drayna, and G.V. Candler, "A Parallel Unstructured Implicit Solver for Hypersonic Reacting Flow Simulation," in *17th AIAA Computational Fluid Dynamics Conference, AIAA 2005-4867*, Toronto, Ontario, 2005.

[22] S. Gordon and B.J. McBride, Computer Program for Calculation of Complex Chemical Equilibrium and Applications: I. Analysis, Oct 1994.

[23] B.J. McBride and S. Gordon, Computer Program for Calculation of Complex Chemical Equilibrium Compositions and Applications: II. Users Manual and Program Description, June 1996.

[24] R. Gosse, D. Callaway, M. Reeder, I. Nompelis, and G. Candler, "Validation of an Equilibrium Ablation CFD Solver with Low Temperature Ablation Experiments Using Dry ice," in *4th Symposium on Integrating CFD and Experiments in Aerodynamics*, Von Karman Institute, Rhode-Saint-Genese, 2009.